

## Article

# Evaluating Electrochemical Properties of Layered $\text{Na}_x\text{Mn}_{0.5}\text{Co}_{0.5}\text{O}_2$ Obtained at Different Calcined Temperatures

Le Minh Nguyen<sup>1</sup>, Van Hoang Nguyen<sup>1,2,\*</sup>, Doan My Ngoc Nguyen<sup>1,3</sup>, Minh Kha Le<sup>2,3</sup>, Van Man Tran<sup>1,2,3</sup> and My Loan Phung Le<sup>1,2,3</sup>

<sup>1</sup> Applied Physical Chemistry Laboratory (APCLAB), VNUHCM-University of Science, Ho Chi Minh City 700000, Vietnam

<sup>2</sup> Viet Nam National University Ho Chi Minh City (VNUHCM), Ho Chi Minh City 700000, Vietnam

<sup>3</sup> Department of Physical Chemistry, Faculty of Chemistry, VNUHCM-University of Science, Ho Chi Minh City 700000, Vietnam

\* Correspondence: nvhoang@hcmus.edu.vn

**Abstract:** P-type layered oxides recently became promising candidates for Sodium-ion batteries (NIBs) for their high specific capacity and rate capability. This work elucidated the structure and electrochemical performance of the layered cathode material  $\text{Na}_x\text{Mn}_{0.5}\text{Co}_{0.5}\text{O}_2$  (NMC) with  $x \sim 1$  calcined at 650, 800 and 900 °C. XRD diffraction indicated that the NMC material possessed a phase transition from P3- to P2-type layered structure with bi-phasic P3/P2 at medium temperature. The sodium storage behavior of different phases was evaluated. The results showed that the increased temperature improved the specific capacity and cycling stability. P2-NMC exhibited the highest initial capacity of 156.9  $\text{mAh}\cdot\text{g}^{-1}$  with capacity retention of 76.2% after 100 cycles, which was superior to the initial discharge capacity of only 149.3  $\text{mAh}\cdot\text{g}^{-1}$  and severe capacity fading per cycle of P3-NMC, indicating high robust structure stability by applying higher calcination temperature. The less stable structure also contributed to the fast degradation of the P3 phase at high current density. Thus, the high temperature P2 phase was still the best in sodium storage performance. Additionally, the sodium diffusion coefficient was calculated by cyclic voltammetry (CV) and demonstrated that the synergic effect of the two phases facilitate the sodium ion migration. Hard carbon || P2-NMC delivered a capacity of 80.9  $\text{mAh}\cdot\text{g}^{-1}$  and 63.3% capacity retention after 25 cycles.

**Keywords:** calcinated temperature; electrochemical performance; sodium-ion batteries;  $\text{Na}_x\text{Mn}_{0.5}\text{Co}_{0.5}\text{O}_2$ ; P-type layered structure



**Citation:** Nguyen, L.M.; Nguyen, V.H.; Nguyen, D.M.N.; Le, M.K.; Tran, V.M.; Le, M.L.P. Evaluating Electrochemical Properties of Layered  $\text{Na}_x\text{Mn}_{0.5}\text{Co}_{0.5}\text{O}_2$  Obtained at Different Calcined Temperatures. *ChemEngineering* **2023**, *7*, 33. <https://doi.org/10.3390/chemengineering7020033>

Academic Editor: Lucun Wang

Received: 23 February 2023

Revised: 25 March 2023

Accepted: 31 March 2023

Published: 10 April 2023



**Copyright:** © 2023 by the authors. Licensee MDPI, Basel, Switzerland. This article is an open access article distributed under the terms and conditions of the Creative Commons Attribution (CC BY) license (<https://creativecommons.org/licenses/by/4.0/>).

## 1. Introduction

The planet warming due to the greenhouse gases exhausted from burning fossil fuels is the primary motivation for switching to renewable energy sources and electricity. In this context, electrochemical energy storage technologies such as rechargeable batteries, which are large storage capacity, easy to install and low cost, are crucial to adapt to the interruption of energy sources. For a long time, lithium-ion batteries (LIBs) have been the dominant power sources for various electronic and electric devices serving every aspect of modern life. Recently, the expansion of the electric vehicles market required more lithium-ion cells to produce enormous energy to ensure proper travel distance. Despite the large number of lithium-ion cells consumed worldwide and growing steadily every year, the predicted shortfall of lithium resources is still a massive challenge for the stability of LIBs uses and the downfall of its price [1]. Therefore, alternative power sources that lower costs and use more abundant and sustainable elements are ever needed. Many researchers were interested in LIB analogs using alkaline and earth elements such as sodium, potassium, aluminum and magnesium. Among them, sodium-ion batteries (SIBs) gained high maturity and were poised to commercial. Sodium-ion batteries' price will be lower than their lithium counterparts because of the abundance of raw materials, including sodium and metal

elements [2]. However, the batteries' currently low energy density, about half of LIBs, limits their applications primarily to household and stationary markets.

Improvement in component engineering, especially cathode electrodes, is expected to improve the energy density of SIB. The aim of achieving high energy density SIBs could be gained by using layered structure oxides that conventionally possess high specific capacity. Sodium transition oxides typically crystallize in O3-type and P2-type layered structures, as named by Delmas and co-workers [3], in which the sodium ions were accommodated at octahedral and prismatic sites, respectively. P2-type materials give good reversible capacity, rate performance and longer cycle life compared to O3-type ones due to higher sodium diffusibility [4–10]. The unitary compounds such as  $\text{Na}_x\text{MnO}_2$  and  $\text{Na}_x\text{CoO}_2$  containing only one transition metal in the repeating  $(\text{MO}_2)_n$  sheets were intensively investigated [11,12], but their poor performance prevented them from being considered as cathode materials for SIBs. Introducing extra ions through substitution and doping was verified to improve the electrochemical properties via synergistic effect. Up to now, abundant multicomponent materials with P2-type layered structures were evaluated during the development of cathode materials for SIBs [4–10].

Among several combinations built for sodium insertion cathode such as Fe-Mn, Ni-Mn, Ni-Mn-Co, Fe-Ni-Mn, Mn-Co incorporation is attractive for its specific capacity and rate capability [13–21]. For instance, P2- $\text{Na}_{2/3}[\text{Mn}_{0.8}\text{Co}_{0.2}]\text{O}_2$  illustrated excellent electrochemical performance with a capacity of about  $175 \text{ mAh}\cdot\text{g}^{-1}$  at 0.1C, and over 90% of its initial capacity remained after 300 cycles at 0.1C and 10C [22]. For sodium-deficient layered cathodes, P3 and P2 were low and high-temperature phases, respectively [23]. Typically, Chen and co-workers reported the preparation of P2- $\text{Na}_{0.67}\text{Co}_{0.5}\text{Mn}_{0.5}\text{O}_2$  and P3/P2- $\text{Na}_{0.66}\text{Co}_{0.5}\text{Mn}_{0.5}\text{O}_2$  at 950 °C and 800 °C, respectively, through a facile and straightforward sol-gel route [19,24]. The P2-phase material delivered a high discharge capacity of  $147 \text{ mAh}\cdot\text{g}^{-1}$  at 0.1C rate and excellent cyclic stability with nearly 100% capacity retention over at least 100 cycles at 1C [19]. The P2/P3-phase material exhibited an impressively higher discharge capacity of  $156.1 \text{ mAh}\cdot\text{g}^{-1}$  at 1C in the voltage range of 1.5–4.3 V [24]. It was noticed that a change in synthesis temperatures affected the macro and nanostructure of the cathode materials related to the electrochemical properties. The two phases intergrowth cathodes showed the improvement in electrochemical performance but the proper ratio of the two phases was not considered.

In this work, we evaluated the structure and the electrochemical properties relationship of  $\text{Na}_x\text{Mn}_{0.5}\text{Co}_{0.5}\text{O}_2$  (NMC) obtained at 650, 800 and 900 °C. We started from a sodium/transition element ratio of unity that was the same as the O3-type phases to lower the mixture's temperature and improve the diffusion in solid state reaction. XRD analysis of the samples indicated that the phase transformation from P3 to P2 phase with intermediate P3/P2 phase coexist as the calcination temperature increased. The electrochemical evaluation suggested that high temperature was better for this material to maximize performance in SIBs due to its own structure stability. Additionally, the synergic effect of two-phase coexist in the P3/P2-NMC enhanced the sodium migration. Full-cell was made using P2-NMC, as the cathode delivered the initial discharge capacity of  $80.9 \text{ mAh}\cdot\text{g}^{-1}$  and remained 63.3% of that value after 25 cycles.

## 2. Materials and Methods

$\text{NaMn}_{0.5}\text{Co}_{0.5}\text{O}_2$  (NMC) was prepared by the conventional solid-state reaction. The starting precursor mixture including  $\text{Na}_2\text{CO}_3$  (Merck, >99%),  $\text{MnCO}_3$  (Sigma-Aldrich, >99%) and  $\text{Co}(\text{NO}_3)_2\cdot 6\text{H}_2\text{O}$  (Sigma-Aldrich, >99%) in a Na/Mn/Co ratio of 2.1:1:1, respectively, was mixed with 1 mL distilled water to make a homogeneous slurry. The slurry was stored for about 30 min to stable and was then heated at 500 °C for 12 h in the air to decompose before being grounded to obtain precursor powder. The next heat treatment step was calcinating the precursor bronze between 650 °C and 900 °C for 12 h in the Ar atmosphere to gain the final materials. In this step, the materials were removed from the furnace at calcinated temperature to cool rapidly in the air and, then, transferred to an

Ar-filled glovebox (GP-Campus, Jacomex). The final samples were named after the calcined temperatures, which were NMC-650, NMC-800 and NMC-900.

The crystal structure of the synthesized NMC samples was examined using X-ray diffraction performed on D8 Advanced (Bruker) diffractometer equipped with a  $\text{CuK}\alpha$  X-ray source ( $\lambda = 0.15418$  nm). The measurement was conducted in a  $2\theta$  angle range from  $10^\circ$  to  $70^\circ$  with  $0.02^\circ/\text{step}/0.25$  s scan rate. In addition, the lattice parameters were obtained from Rietveld refinement using Material Studio (version 2017).

The Raman spectrum was collected on Xplora One Raman Spectrometer (Horiba) equipped with  $\text{Ar}^+$  laser with a wavelength of 532 nm. The morphologies of NMC materials were evaluated using FE-SEM S-4800 (Hitachi) scanning electron microscope with energy-dispersive X-ray spectroscopy (EDS) coupled optionally to explore the chemical composition and elements distribution.

The cathode electrode was prepared in the Ar-filled glovebox. The as-prepared NMC material, conducting carbon C65 and poly(vinylidene fluoride-co-hexafluoropropylene) (PVDF-HFP) binder in a weight ratio of 80:15:5, respectively, was mixed with N-methyl-2-pyrrolidone (NMP) solvent under magnetic stirring for at least 2 h to make a slurry. Then, the slurry was coated onto technical Al foil, dried at  $80^\circ\text{C}$  in the glovebox before being placed in a vacuum oven at  $100^\circ\text{C}$  for 12 h. Finally, the foil was moved to the glovebox and was punched into round pieces with a diameter of 12.7 mm and mass loading of  $2\text{--}3\text{ mg}\cdot\text{cm}^{-2}$ .

For the anode, commercial hard carbon (Kureha Battery Materials, Tokyo, Japan) (90%), carbon C65 (5%) and carboxymethyl cellulose (CMC) (10% solution in water) were mixed under magnetic stirring for at least 2 h to obtain a homogeneous slurry. The slurry was coated on a Cu foil, dried at  $100^\circ\text{C}$  for 12 h in the vacuum oven and was then punched into round electrodes with 12.7 mm-diameter and mass loading of  $1\text{ mg}\cdot\text{cm}^{-2}$ .

Coin cells CR2032 were used in electrochemical properties characterization. The cells were assembled in the Ar-filled glovebox with the cathode film as working electrode, a circular Na foil as reference and counter electrodes, two Whatman glass fibers (GF/F) as separator, and the electrolyte was a solution of 1 M  $\text{NaClO}_4$  in propylene carbonate (PC) with 2% fluoroethylene carbonate (FEC) additive. The full-cell was assembled using coin cell CR2032 with the same structure as above, but hard carbon was used as the counter electrode.

Electrochemical testing was controlled by multi-channel MPG-2 and VSP battery cycler (Biologic, France). Cyclic voltammetry (CV) was conducted with a scan rate of  $20\text{--}100\ \mu\text{V}\cdot\text{s}^{-1}$  between 1.5 and 4.5 V. Charge–discharge performance was processed in Galvanostatic mode with different C-rate (1C corresponding to a nominal specific capacity of  $150\text{ mAh}\cdot\text{g}^{-1}$ ). Full-cell was cycled with a current density of 1C (that was calculated based on the cathode) between 0.1 and 4.5 V. Electrochemical impedance spectroscopy (EIS) was measured by applying an alternating potential with an amplitude of 10 mV in the frequency range from 1 MHz to 100 mHz at equilibrium potential.

For the XRD analysis to evaluate the structure during charging, the cells were charged by a current density of C/20 for 5 cycles and were then rested for at least 3 h before being opened in the glovebox to obtain the cathode films. The cathode films were washed in dimethyl carbonate (DMC) at least three times before being dried in a hot plate at  $100^\circ\text{C}$  and sealed. They were subjected to XRD analysis on D8 Advance (Bruker) coupled with a  $\text{CuK}\alpha$  source ( $\lambda = 1.5814\ \text{\AA}$ ) and the scan rate was  $0.02^\circ/\text{step}/0.25$  s.

### 3. Results

Figure 1 shows the thermal behavior of the precursor between room temperature and  $1000^\circ\text{C}$  in the dry air. It was observed in the TGA curve that the precursor exhibited several mass losses, which started from about  $80^\circ\text{C}$  and lasted until the end of the investigated temperature range. The DSC curve displayed a sloping curve, which demonstrated endothermic reactions. The first mass loss of about 2% with a slope at roughly  $83^\circ\text{C}$  in the TGA curve was of water desorption, corresponding to the first peak in the DSC curve.

Additionally, the acceleration of mass loss was observed as starting from roughly 200, 550 and 750 °C, corresponding to the continued decomposition of residual anions/metal salts, oxygen removal, and sodium evaporation under an oxidation atmosphere. During this time, the solid-state reaction between the components was also activated, and the reconstruction of the precursor happened. It was noticed in the TGA that the decomposition seemed to finish at around 800 °C, where no significant mass loss was observed.

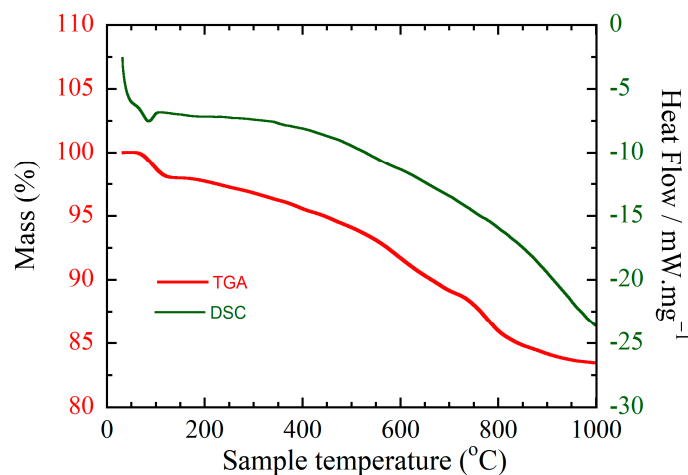


**Figure 1.** TG/DSC curves of the precursors.

The XRD of the samples at 650 °C, 800 °C and 900 °C (Figure 2a–c) revealed the structure evolution from P3 to P2 during the temperature increase and that the mass loss on TGA might have come with structure reconstruction. For instance, the P3-type layered structure was observed in the sample at 650 °C, while the second phase P2 was seen in the samples above 800 °C. The formation of P3 phase was at a lower temperature than the previously studied P3-phase cathodes that calcined at 700/750 °C [25–27]. The P3 structure obtained Cm space group (PDF#00-054-0839). On the other hand, the P2-type layered structure with P6<sub>3</sub>/mmc space group (PDF#01-070-3726) was gained in the sample NMC-900. The presence of P2 phase at a high temperature of 900 °C coincided with previous studies because the phase was more stable at high temperatures than P3 phase [23,28,29].

The Rietveld refinement results for structure analysis of the materials shown in Figure 2a–c revealed a good match between the simulation and the experiment patterns with a depleted different curve. The reasonably low  $R_{wp}$  (11.23, 9.38, and 6.64% for the calcinated temperature of 650, 800 and 900 °C, respectively) showed that the higher temperature exhibited less mismatch due to higher crystallinity. In addition, it was observed that almost all the samples were high purity because of the absence of unidentified peaks. The Rietveld refinement results also indicated that the percentage of the P2 phase was slightly higher compared to the P3 phase when calcined at 800 °C. Table 1 lists the lattice parameters of different phases in the materials. The calculated results of a, c axes and the volume V did not possess significant differences in the same phases.

The Raman spectra for the three samples with different temperatures shown in Figure 2d were similar to those obtained from Na<sub>2/3</sub>Co<sub>2/3</sub>Mn<sub>2/3</sub>O<sub>2</sub> [30], but the peaks shifted forward due to the difference in sodium concentration and element composition. The spectra presented two peaks at 630 and 581 cm<sup>-1</sup>, which were attributed to the deformation and symmetric stretching vibrations (A<sub>1g</sub> and E<sub>g</sub>, respectively) of metal-oxygen (Mn/Co–O) bonds of Mn/CoO<sub>6</sub> octahedral in layered Na-metal transition oxides [30,31]. The peaks at 488 and around 800 cm<sup>-1</sup> could be explained by impurity (other phase structure and metal oxides) or sublattice. It was induced that the P3 and P2 layered structure of NMC material were probably distinguishable by Raman spectra, because of the different between the spectra of the samples calcined at 650 and 900 °C. Namely, the peak splitting at 488 cm<sup>-1</sup> and the peak shifting from 800 cm<sup>-1</sup> to high wavelength were seen in the spectra of the 900 °C sample, which were expected to differ the P2 phase from the P3 phase.

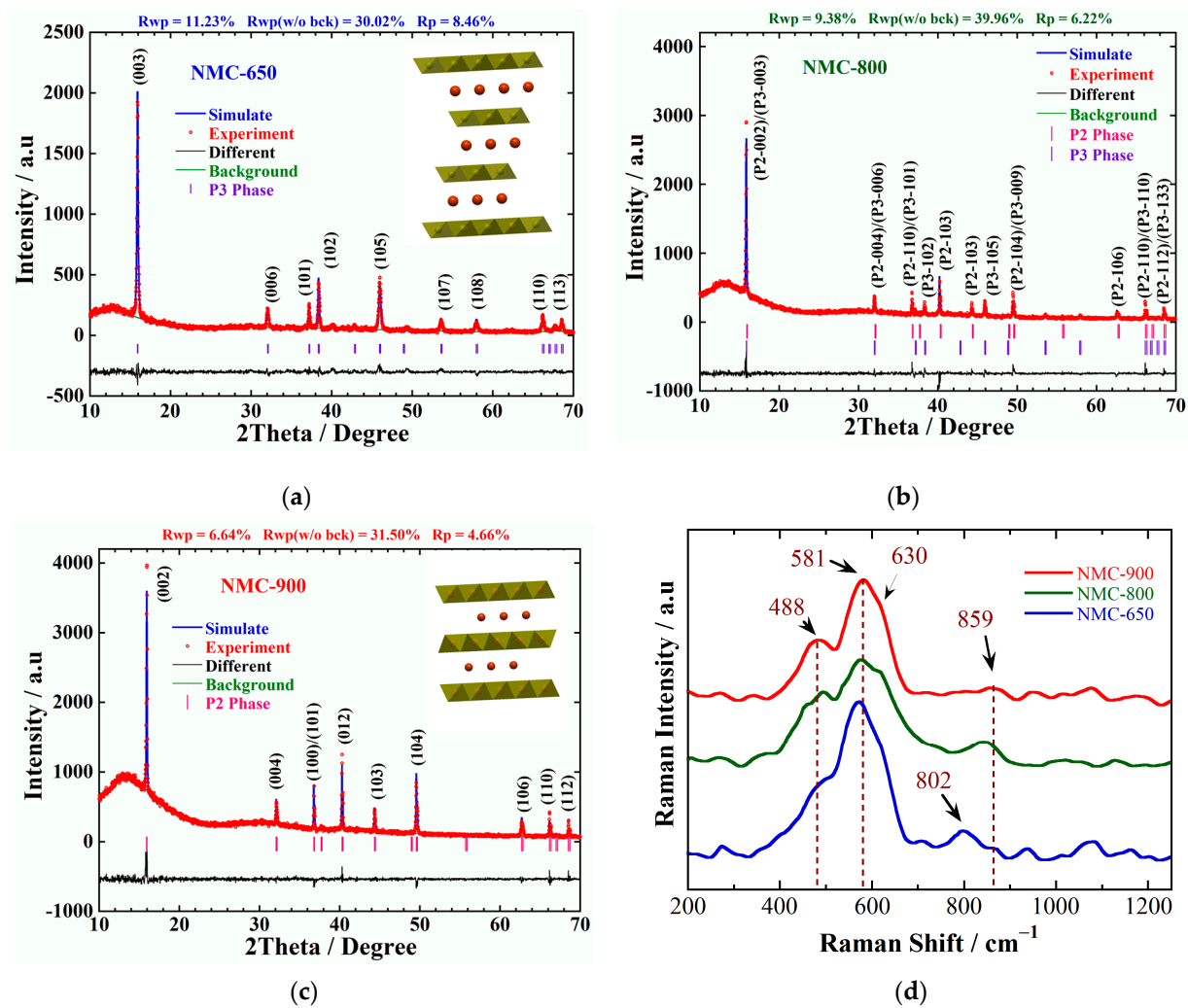


**Figure 2.** Rietveld refinement results of the NMC materials obtained at various calcined temperatures (a) NMC-650, (b) NMC-800 and (c) NMC-900, (d) Raman spectra of the synthesized materials. Inset of (a,c) shows the schematic of crystal structures of P3 and P2-type layered oxide, respectively.

**Table 1.** Crystallographic parameters of  $\text{Na}_x\text{Mn}_{0.5}\text{Co}_{0.5}\text{O}_2$  materials prepared at different calcination temperatures of 650, 800 and 900 °C.

Sample ID	Notation	Space Group	Lattice Parameters			Weight Percentage (Rietveld)
			a (Å)	c (Å)	V (Å <sup>3</sup> )	
NMC-650	P3	Cm	2.831	16.530	114.730	100.00
NMC-800	P2	P63/mmc	2.823	11.192	77.258	58.60
	P3	Cm	2.827	16.735	115.799	41.40
NMC-900	P2	P63/mmc	2.825	11.178	77.279	100.00

SEM images of P2- and P3-NMC (Figure 3) showed irregular-shaped polygonal particles with a size of a few micrometers made up of the aggregation of flaky particles with smaller dimensions. The sample morphologies were almost similar, but the particle size of P2-NMC was relatively larger than P3-NMC due to higher calcined temperature. EDS images of element contribution confirmed the presence of all essential elements in the samples.

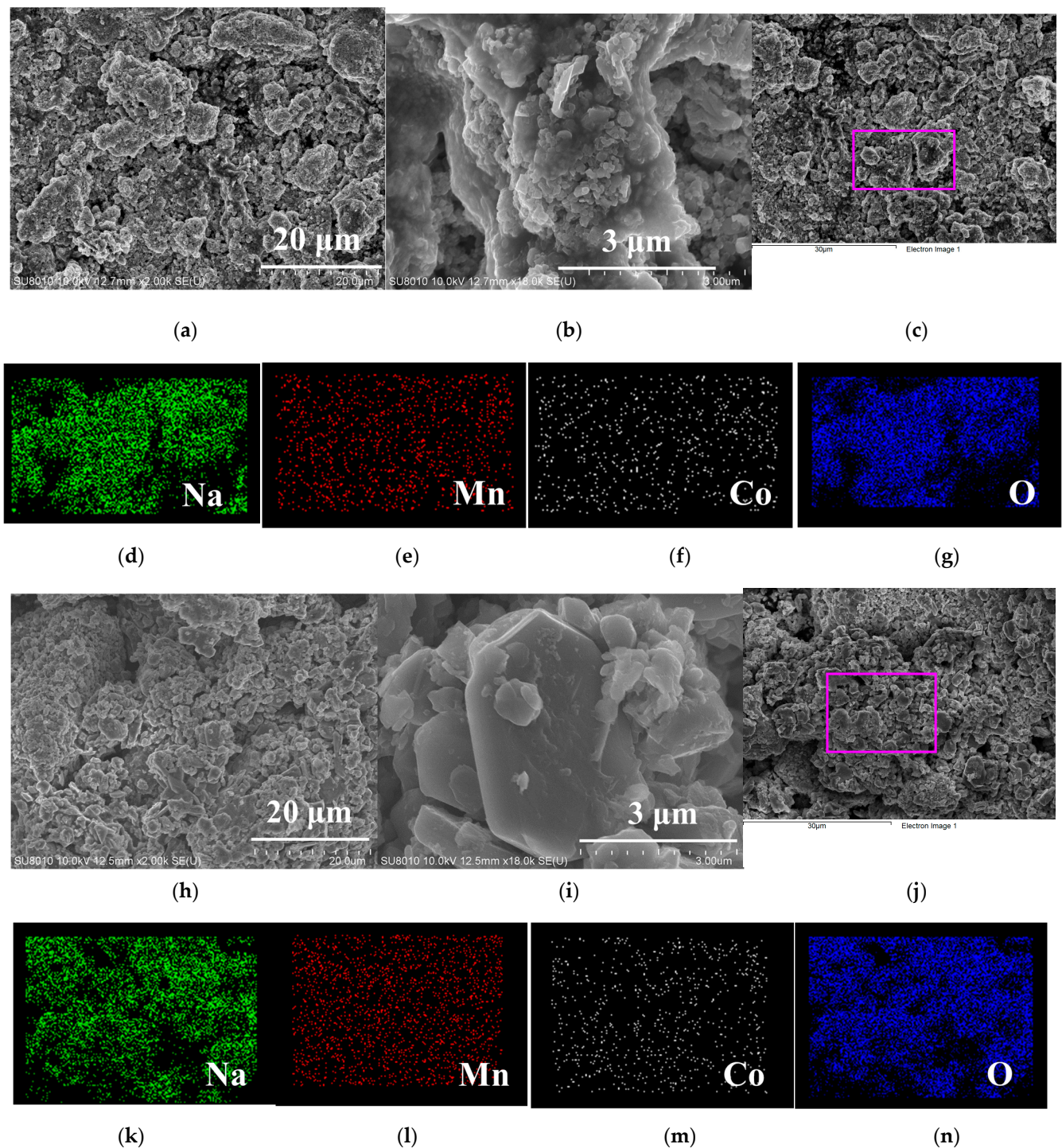


**Figure 3.** (a–c) SEM images of NMC material calcined at 650 °C and (d–g) EDX mapping results of area in the SEM image (c); (h–j) SEM images of NMC material calcined at 800 °C and (k–n) EDX mapping results of area in the SEM image (j).

The electrochemical properties characterization of the materials is presented hereafter. CV curves of the synthesized samples are given in Figure 4a. Typically, the CV curves showed many peak couples corresponding to several successive phase transitions and structure evolution during sodiation/desodiation. For the voltage range 1.5 to 4.5 V, the CV curves could be divided into three regions at about 2.7 and 4.3 V knots. The first and the second regions had peaks that mainly contributed to  $\text{Mn}^{4+}/\text{Mn}^{3+}$  and  $\text{Co}^{4+}/\text{Co}^{3+}$  redox couples, respectively, while the last one contributed by  $\text{Co}^{4+}/\text{Co}^{3+}$  redox reaction and

decomposition of the electrolyte when being charged up to 4.5 V. Additionally, the CV curve of the sample calcined at 900 °C was smoother, and the peak couples were rather more reversible. It could be noticed that the CV curve of NMC-800 was a superposition of the others because both P3 and P2 phases existed. In general, the CV feature of P-type layered NMC was almost the same, regardless of the difference in the crystal lattice, probably because they had the same redox species and composition.

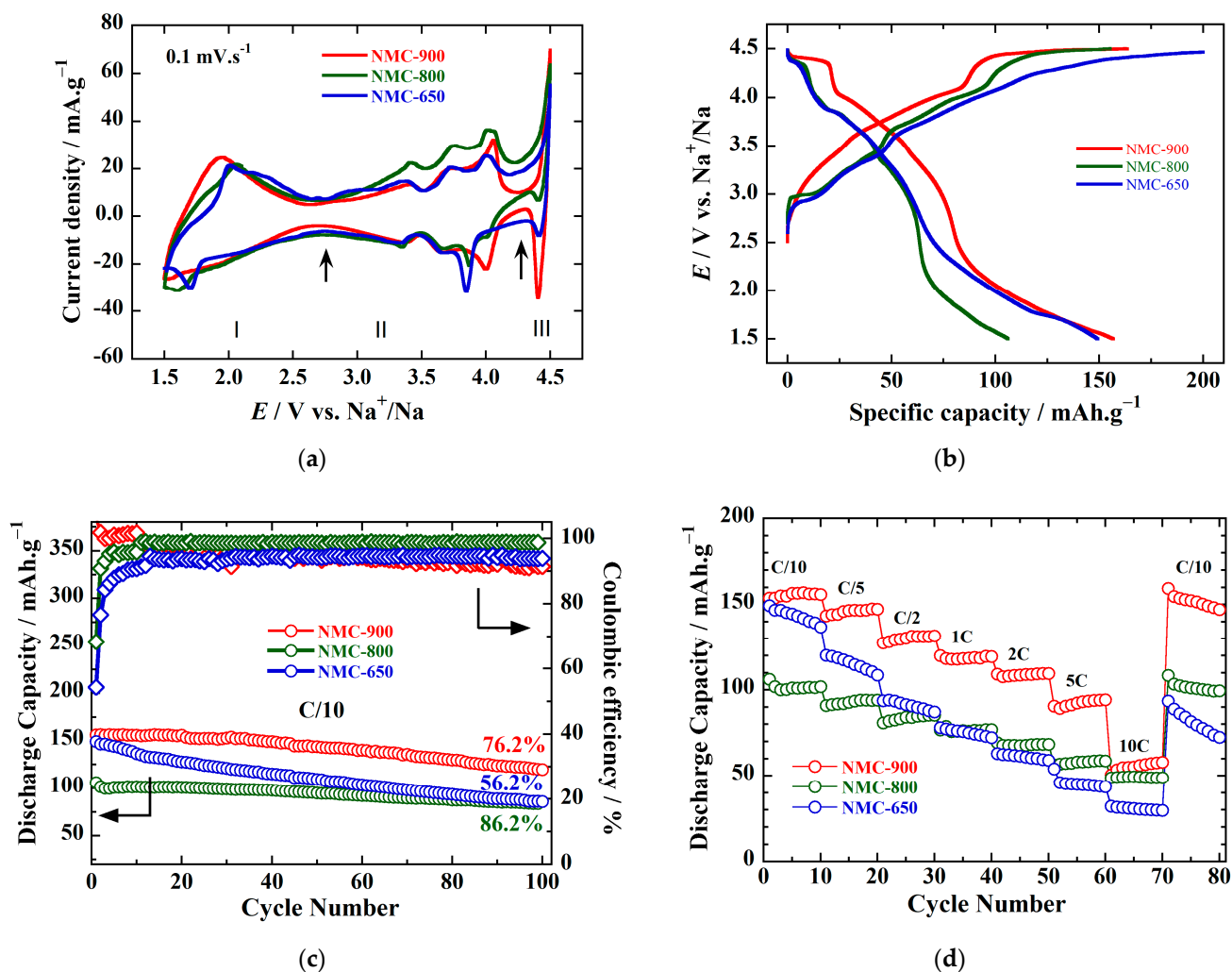


**Figure 4.** (a) Cyclic voltammogram of NMC materials in 1.5–4.5 V voltage windows at a scan rate of  $100 \mu\text{V}\cdot\text{s}^{-1}$ . (b) The first charge–discharge voltage profiles, (c) evolution of capacity and Coulombic efficiency with cycle number of the material cycled in a voltage range of 1.5–4.5 V and (d) rate capability in the same voltage limit.

The galvanostatic charge/discharge curves of the initial cycle are shown in Figure 4b. All the samples showed characteristic voltage profiles that were rather alike with relatively high discharge capacities, coinciding with the electrochemical behavior shown in CV curves. However, the samples NMC-650 and NMC-800 exhibited high irreversible capacity in the first cycle, resulting in low Coulombic efficiency with the value of about 74.2% and 68.5% for NMC-650 and NMC-800, respectively. It could be noticed that NMC-800, with a complex composition including P3 and P2 phase, presented an even higher irreversible capacity than the P3 phase and P2 phase components. Meanwhile, the sample NMC-900 exceptionally displayed a nearly reversible charge/discharge cycle with Coulombic efficiency of about 96.6%. In general, the P-phases with sodium deficiency typically displayed high Coulombic efficiency above 100% [4,8,19]. Thus, the materials obtaining P2 phase with a high sodium

content of 1, such as the O3 phase, gained high Coulombic efficiency due to the excess Na<sup>+</sup> ions that were possible due to the electrolyte.

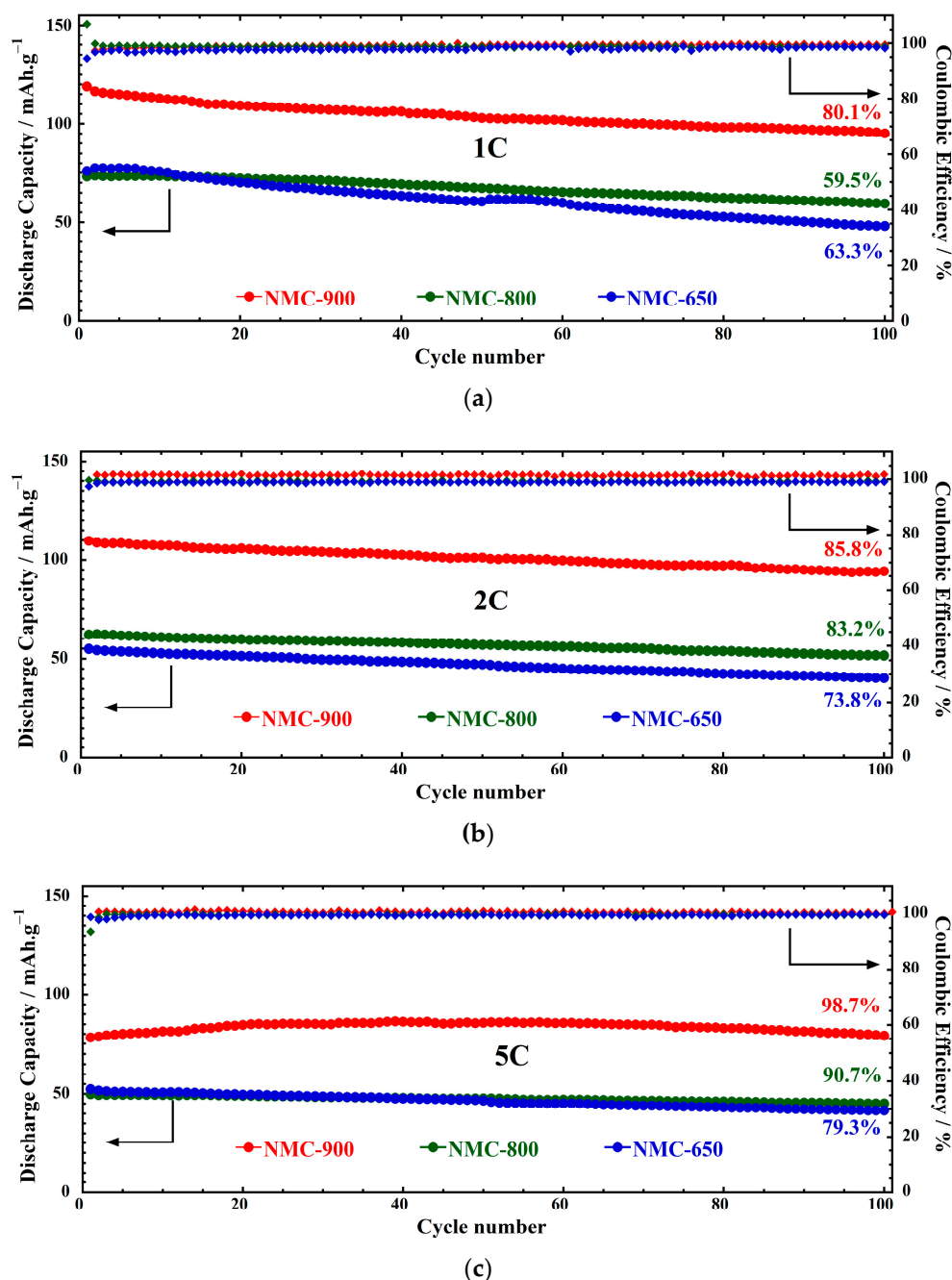
Moreover, the redox couple Co<sup>4+</sup>/Co<sup>3+</sup> was activated when charged to a high cutoff voltage and contributed to the large irreversible charge capacity of the samples NMC-650 and NMC-800. For the sample NMC-900, the huge sodium loss via evaporation due to high calcined temperature reduced the Coulombic efficiency. As a result, the initial discharge capacity of 149.3, 106.2 and 156.9 mAh·g<sup>-1</sup> were obtained for the sample NMC-650, NMC-800 and NMC-900, respectively; hence, the Coulombic efficiency were 74.6, 68.4 and 89.8%, respectively.

Figure 4c shows the capacity and Coulombic efficiency of the samples during long-term charge–discharge. It was observed that the samples NMC-800 and NMC-900 attained stable cycling that slightly changed in capacity for each cycle. The sample NMC-900 remained a capacity higher than the others, with a capacity retention of 76.2% after 100 cycles. On the other hand, the capacity of NMC-650 reduced gradually and the capacity retention was about 56.2% after 100 cycles. The sample NMC-800 had a two-phase component, but capacity retention was the best of the three, with a value of 86.2% after 100 cycles. Additionally, the NMC-800 and NMC-900 samples possessed a slightly capacity increase in the first dozen cycles that could be assigned to the increase in active surface and active site of sodium that were mentioned elsewhere [32,33] and obviously contributed to the higher capacity retention of these materials. This could be related to the enhanced electrolyte permeability and the reconstruction of the electrode and the interface.

The rate capability of the samples is illustrated in Figure 4d. It was observed that the three samples displayed acceptable rate capability. Of the three, the samples NMC-650 and NMC-800 exhibited good capacity retention in which the capacities dropped steadily and were negligible when the current density increased from C/10 to 10C. Meanwhile, the capacity of NMC-900 fell significantly at the high current density of above 5C. However, when the current density returned to C/10, only NMC-650 showed a sharp decrease in capacity compared to the initial value at the same current density. Furthermore, both NMC-900 and NMC-800 possessed the capacity increase in the first few cycles at different C-rates. The extended capacity could contribute to the high capacity recovery that was even higher than the capacity at C/10 at the beginning when the current returned to C/10 after cycling at different C-rates.

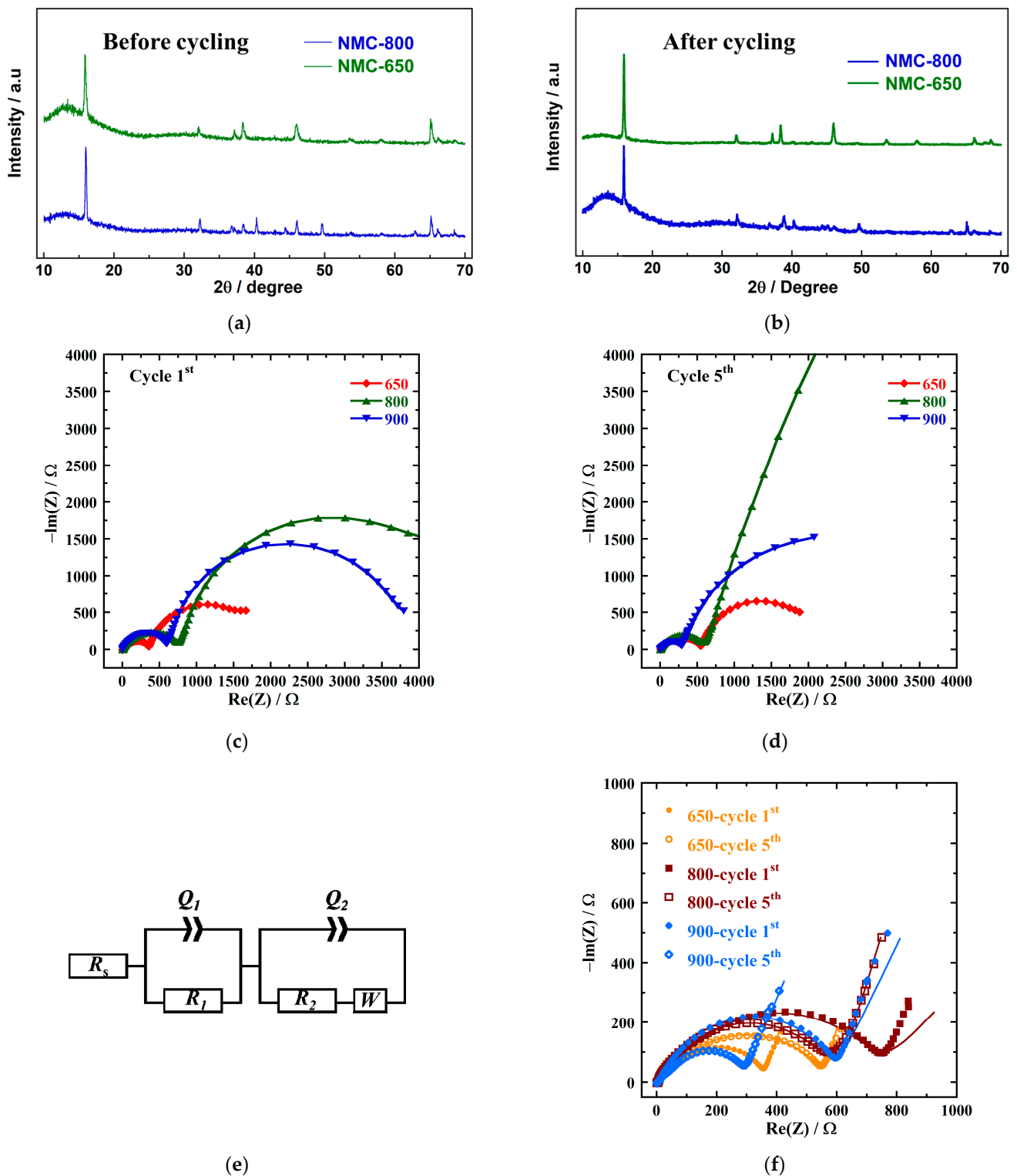
The long-term charge–discharge at higher current density was applied to characterize the stability of electrodes (Figure 5). Generally, the capacities of the three samples were stable during the cycle with low-capacity decay that coincided with the rate capability test. It was observed that the capacity retention at the high rate was better because of shortened retention time in high voltage regions and the contribution of capacity from the high voltage redox couple [21]. NMC-650 displayed insufficient capacity and capacity retention compared to the other two in all the test conditions, while NMC-900 performed the best. Additionally, the Coulombic efficiency of approximately 100% was gained by all the samples at various rates.

Figure 6a,b show the XRD patterns of the bare electrodes NMC-650 and NMC-800 and the electrodes at the fifth cycle. Compared with the XRD of the bare NMC-650 and NMC-800 shown in Figure 2a,b, respectively, it could be seen that the samples retained the original structure and phase component, revealing the good structure stability. Furthermore, the fading of high redox couples during the first several cycles seemed not to be correlated with the appearance of a new phase or structure changes. Thus, the results demonstrated that P-type layers displayed high structural stability. Our previous work also indicated that NMC-900 could remain a P2-type layered structure after 50 cycles of charging–discharging [21]. Typically, P3 phase exhibits phase transformation P3-O3 near the end of discharge [34–36], while P2 phase remains its structure during the cycling [19,37]. Further work will be carried out to analyze the phase transition of the different phases during the cycling.



**Figure 5.** Electrochemical performances of NMC cathodes upon cycle tests in the range of 1.5–4.5 V at (a) 1C, (b) 2C and (c) 5C, respectively.

EIS spectra of the electrodes were also collected at the beginning of the cycling test and at the fifth cycle as shown in Figure 6c,d. The EIS spectra showed a semicircle at high and medium frequencies of the charge transfer resistance and one huge semicircle at low frequency due to ion diffusion in the porous electrode [38]. Typically, the high frequency charge transfer process could be simulated by a single Randles circuit including a capacitance and a resistance in series, while the low frequency semicircle could be simulated by a series combination of capacitances and resistors [39]. The equivalent circuit used to simulate the charge transfer resistance is shown in Figure 6e, showing two charge transfer processes which, in turn, occurred on the cathode interface film ( $R_1$ ) and cathode electrolyte interface ( $R_2$ ). Table 2 provides the value of resistance parameters obtained after simulation.



**Figure 6.** XRD patterns of the electrodes obtained (a) before and (b) after cycling. EIS spectra of the electrode NMC-650, NMC-800 and NMC-900 obtained at (c) the first and (d) the fifth cycles. (e) Equivalent circuit that use to fit the EIS results and (f) Nyquist plot for the electrodes with a frequency range from  $10^6$  to 0.1 Hz. The measurement data are shown by the dots and the fitting curves are presented by the solid lines.

**Table 2.** Resistance parameters obtained from EIS fitting.

Sample ID		$R_s$	$R_1$	$R_2$	Total Charge Transfer Resistance
NMC-650	1st	7.995	53.07	297.1	350.2
	5th	5.605	69.17	490.8	560.0
NMC-800	1st	5.053	65.02	657.2	722.2
	5th	4.809	23.75	543.6	567.4
NMC-900	1st	5.364	82.32	498.6	580.2
	5th	6.526	50.11	226.3	276.4

As seen in Table 2, the  $R_s$  values did not change too much, while the charge transfer resistance  $R_1$  and  $R_2$  changed in a similar trend. The sum of  $R_1$  and  $R_2$ , the total resistance for the high and medium frequency, showed different changes in the three electrodes and tended to decrease, in turn, (NMC-650 > NMC-800 > NMC-900) after five cycles. The change in the electrode interface such as the electrolyte decomposition to form cathode thin film, the reconstruction of the electrodes' morphology and the change in the electrodes' electronic and electrochemical properties reflected the charge transfer process. In general, the change of charge transfer resistances was consistent with the cycling stability of the electrodes. Specifically, the increase in charge transfer resistance and the resulting poor performance of the NMC-650 electrode suggested that the capacity degradation was consistent with the fast impedance buildup. Oppositely, the tendency of decrease in charge transfer resistances at the fifth cycle revealed an improvement in the kinetic of charge transfer at the NMC-800 and NMC-900 electrodes' interfaces.

The kinetic of sodium ion intercalation/deintercalation in the structure that correlates to the performance of the electrode could be evaluated by CV conducted at various scan rates. Figure 7a–c shows that the CV curves of the electrodes at the scan rate varied from 10 to 250  $\mu\text{V}\cdot\text{s}^{-1}$ . Several redox peaks on the CV could be assigned to  $\text{Mn}^{4+}/\text{Mn}^{3+}$  and  $\text{Co}^{4+}/\text{Co}^{3+}$  redox couples together with phase transition and evolutions during sodium intercalation/deintercalation [5,40]. As one can see, with the scan rate increases, the redox peaks' intensity increased but the CV profiles were almost unchanged, indicating high redox reversibility and coinciding to the prominent rate capability of the electrodes.

The plot of peak current intensity versus square root of scan rate was used to determine whether the redox reaction was diffusion controlled [41]. The peak intensity of the oxidation peak and reduction peak located at around 4 V were plotted versus the square root of the scan rate and illustrated in Figure 7d, for instance. The fitted lines indicated that the linear relationship was satisfied, and so, the forward and reverse reactions were diffusion controlled. The feature was also recognized using the fitting way with other peaks in the CV profiles. Therefore, the diffusion coefficients can be calculated according to the Randles–Sevcik equation [41]:

$$I_p = (2.69 \times 10^5)n^{2/3}AC_0D^{1/2}\nu^{1/2} \quad (1)$$

where  $I_p$  is the peak current (A),  $n$  is the number of exchange electron,  $A$  is the electrode area ( $\text{cm}^2$ ),  $D$  is  $\text{Na}^+$  diffusion coefficient ( $\text{cm}^2\cdot\text{s}^{-1}$ ) and  $C_0$  is the initial concentration of  $\text{Na}^+$  ion ( $\text{mol}\cdot\text{cm}^{-3}$ ).

The calculated  $D$  values of oxidation peaks and reduction peaks observed in CV profiles were plotted versus the peak position presented in Figure 7e,f, respectively. From the  $D$  values, one could elucidate that NMC-900 possessed the lowest diffusion coefficients, which was around  $10^{-12.8}$ – $10^{-12.0}$   $\text{cm}^2\cdot\text{s}^{-1}$ , and so, the migration of  $\text{Na}^+$  ions was not as favorable compared to the others. Meanwhile, the  $D$  values of the samples NMC-800 and NMC-650 were higher, which was around  $10^{-12.2}$ – $10^{-11.4}$   $\text{cm}^2\cdot\text{s}^{-1}$ , and so, the migration of  $\text{Na}^+$  ion was probably more favorable by the integration of P3/P2 bi-phase than the P2 phase solely. The diffusion coefficient of the P3/P2 bi-phase NMC-800 coincided with the previous study [42]. To explain the notable higher diffusivity of P3/P2 bi-phase, one could agree that the diffusion of  $\text{Na}^+$  ion in the P3 structure is higher than P2 and O3 in

some cases [25,27]. Furthermore, for the sample NMC-800 that exhibited P3/P2 bi-phase integration, the P2 component probably maintained the structure but was electrochemically inactive; so, the NMC-800 performance was not the best of the three, as expected.

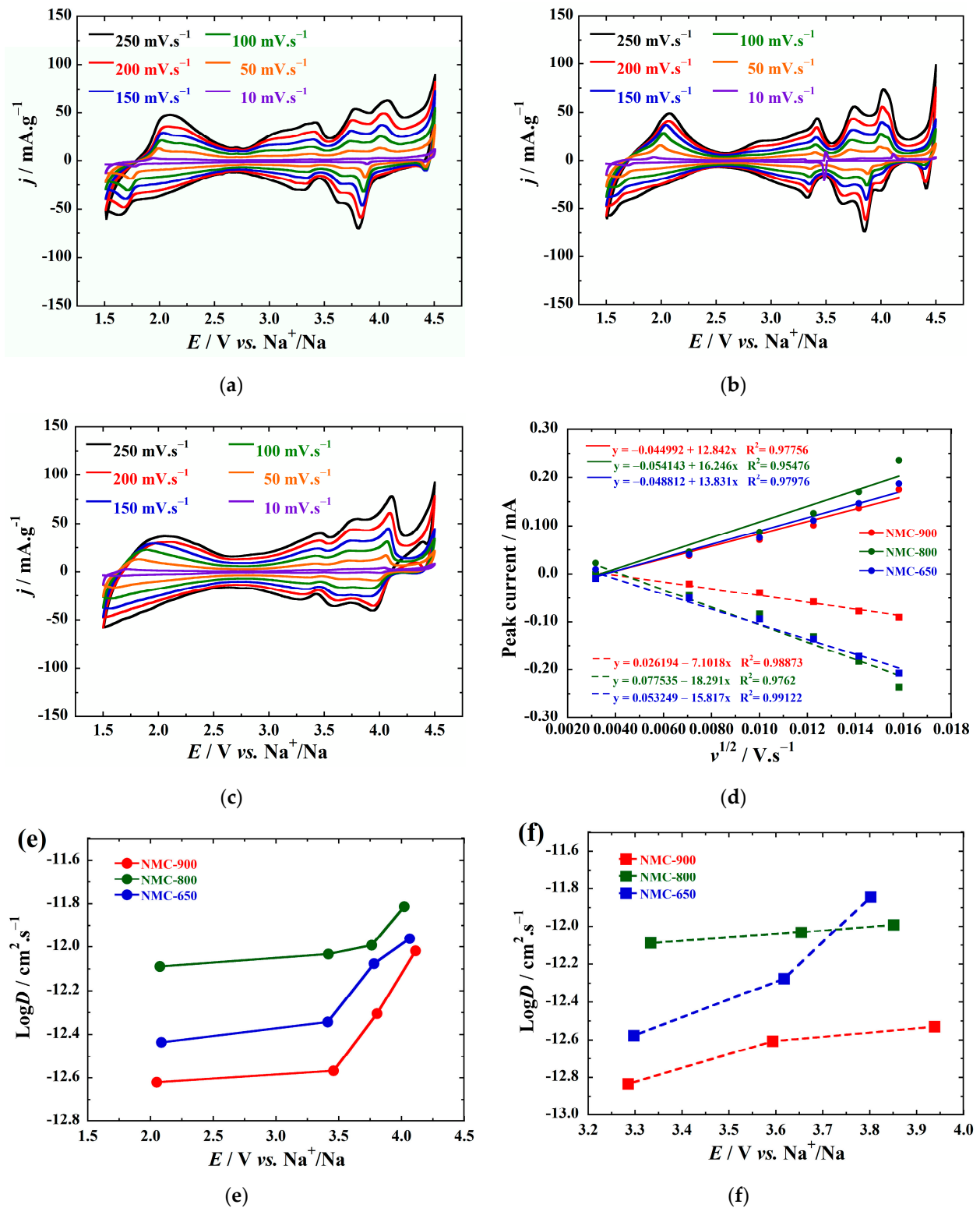


**Figure 7.** Cyclic voltammogram scanned at various scan rates of (a) NMC-900, (b) NMC-800 and (c) NMC-650. (d) The plot of current intensity at a pair of oxidation/reduction peaks is located at about 4 V versus the square root of the scan rate of the samples; The plot of diffusion coefficients calculated at (e) oxidation and (f) reduction peaks.

The performance of P2-NMC was also evaluated in full-cell configuration using hard carbon as the anode (Figure 8). The mass ratio between the cathode and the anode of 1.4 was chosen for the highest capacity. As displayed in Figure 8a, the voltage profile of the full-cell was the combination of the voltage profile of the cathode and the anode. The first charge capacity of about  $151.4 \text{ mAh}\cdot\text{g}^{-1}$  was obtained and was comparable to the corresponding value of the material delivered in the half-cell on the first cycle and was much higher than the discharge capacity of only  $80.9 \text{ mAh}\cdot\text{g}^{-1}$ . This resulted in the low Coulombic efficiency of 51.9%. The irreversible capacity of hard carbon anode leads to the low Coulombic efficiency, so that presodiation techniques were widely used to optimize the performance of full-cells [43–45]. For the following cycles, the Coulombic efficiency varied around 92% and the capacity gradually declines were seen as the results of side reactions of the electrolyte on the electrodes due to wide operation voltage. The capacity retention at 25th cycle was 63.3%.

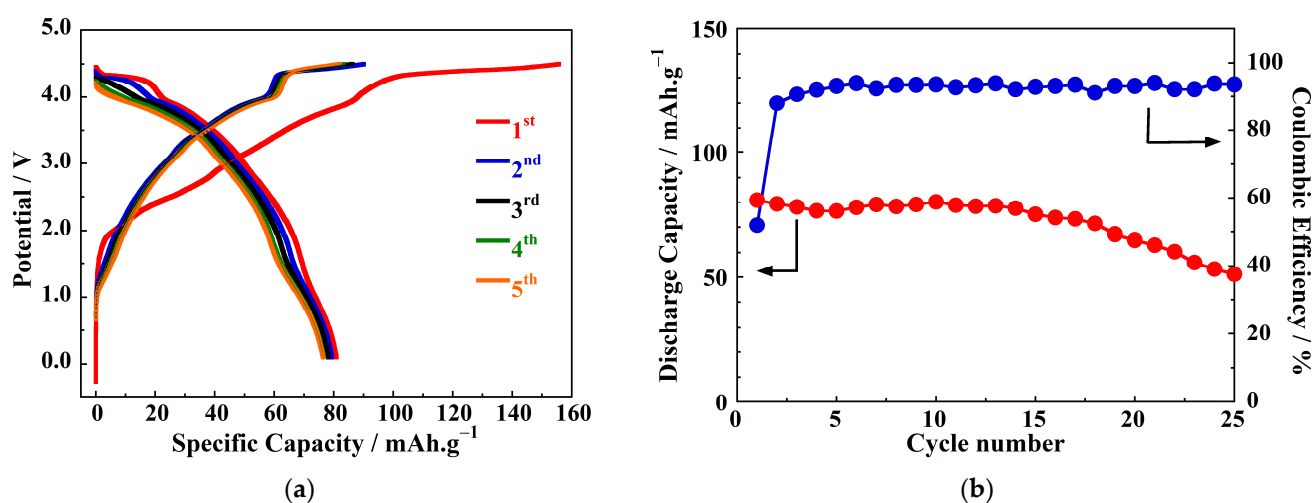


**Figure 8.** Cycling performance of hard carbon || NMC-900 full-cell. (a) The voltage profile and (b) evolution of capacity and Coulombic efficiency with cycle number.

#### 4. Discussion

The P-type layered structures exist within 650–900 °C, given the high thermal stability of the P-phase in the Na-Mn-Co system. Several mechanisms were explored considering the capacity fading of high voltage materials, including intragranular and lattice fracture caused by lattice change during phase transition, surface structural change and irreversible lattice oxygen release [46]. The results indicated that the phase structure had tie connection to the cycling stability that was observed to be improved by elevated temperature. Figure 7e,f show that the P3 phase could have a facile environment for sodium ion conductivity, but poor capacity retention compared to the P2 phase. Additionally, as could be seen on the first cycle (Figure 4b), the sample at low temperature NMC-650 and NMC-800 exhibited a severe side reaction on charge at high voltage plateaus that contributed mainly from the decomposition of the electrolyte and may be assisted by the high active surface and the stability of the electrode surface in the electrolyte. This occurred repeatedly in consecutive cycles, leading to the low Coulombic efficiency of the NMC-650 sample (Figure 4c). The performance of the hard carbon || P2-NMC full-cell was still far below to the half-cell, emphasizing the important role of presodiation techniques of the anode.

For comparison, the electrochemical performance of some electrode materials at high voltage range are listed in Table 3. The Mn-Co system delivered lower specific capacity than other Mn-based systems, but good cycling stability. This demonstrated the role of Co in stabilizing the structure and enhancing the electrochemical performance of the electrode materials as previously reported [47,48].

The two-phase intergrowth cathodes were reported to improve the rate capability and specific capacity contributed by the synergic effect of both components [24,41,49–51].

This work revealed that the P3/P2 integration in NMC-800 was beneficial to capacity retention, but the capacity was lower than the single-phase components, which could be associated, respectively, with the robust intrinsic structure and the severe side reaction of the electrolyte that induced more sodium lost during the solid electrolyte interface (SEI) formation, resulting in relatively higher SEI and charge transfer resistance over others (Figure 6c–e). Further works should be taken to understand the microstructure and surface structure of the bi-phasic electrode to better understand the sodium storage performance.

**Table 3.** Comparison of the electrochemical performance of electrode materials at high cutoff voltage.

	Voltage Range	Specific Capacity (mah·g <sup>-1</sup> )/Current Density	Capacity Retention/Cycle Number	Refs
P2-Na <sub>0.7</sub> Cu <sub>0.2</sub> Fe <sub>0.2</sub> Mn <sub>0.6</sub> O <sub>2</sub>	1.5–4.5 V	~190 (C/10)	~69% (30)	[52]
P2-NaMn <sub>0.5</sub> Fe <sub>0.5</sub> O <sub>2</sub>	2.0–4.3 V	185 (C/10)	60% (50)	[53]
P2-Na <sub>2/3</sub> Ni <sub>1/3</sub> Mn <sub>2/3</sub> O <sub>2</sub>	2.0–4.5 V	133 (~C/10)	42% (50)	[54]
P2-Na <sub>0.66</sub> Mn <sub>0.9</sub> Mg <sub>0.1</sub> O <sub>2</sub>	2.0–4.5 V	152 (~C/5)	71% (100)	[55]
P3-Na <sub>0.9</sub> Ni <sub>0.5</sub> Mn <sub>0.5</sub> O <sub>2</sub>	1.5–4.5 V	102 (1C)	78% (500)	[56]
P2-NaCo <sub>0.5</sub> Mn <sub>0.5</sub> O <sub>2</sub> (This work)	1.5–4.5 V	149 (C/10)	76% (100)	

## 5. Conclusions

In summary, Na<sub>x</sub>Mn<sub>0.5</sub>Co<sub>0.5</sub>O<sub>2</sub> possessed phase transition from P3- to P2-type layered structure when calcinated at 650 and 900 °C with bi-phasic P3/P2 coexisted in a medium temperature of 800 °C. The electrochemical properties examinations indicated that the higher calcinated temperature improved the crystallinity and strongly contributed to the cycling stability and performance. For instance, the sample NMC-900 exhibited the highest specific capacity and capacity retention at high rates that were superior to the others. Meanwhile, the bi-phase P3/P2 NMC-800 delivered the lowest specific capacity, but showed the highest diffusion coefficient, contributing to the high-rate capability and structure stability during sodium intercalation/deintercalation. The results demonstrated that single phases were better for Na<sub>x</sub>Mn<sub>0.5</sub>Co<sub>0.5</sub>O<sub>2</sub> material and P2 phase was preferred in terms of electrochemical performance. Further works should be conducted to understand the electrochemical performance of the bi-phasic P3/P2 NMC-800 that probably benefits and improves the performance of Na-Mn-Co electrode system.

**Author Contributions:** L.M.N., suggested the idea and methods, conducted the experiment and prepared the manuscript; D.M.N.N., conducted the experiment and prepared the manuscript; V.H.N., suggested the idea and methods and edited and submitted the manuscript; M.K.L., V.M.T. and M.L.P.L., lecture contribution to complete the manuscript. All authors have read and agreed to the published version of the manuscript.

**Funding:** This research was funded by University of Science, Viet Nam National University Ho Chi Minh City, under grant number HH 2021-03.

**Informed Consent Statement:** Not applicable.

**Data Availability Statement:** The data that support the findings of this study are available from the authors, upon reasonable request.

**Conflicts of Interest:** The authors declare no conflict of interest.

## References

1. Palomares, V.; Serras, P.; Villaluenga, I.; Hueso, K.B.; Carretero-González, J.; Rojo, T. Na-ion batteries, recent advances and present challenges to become low cost energy storage systems. *Energy Environ. Sci.* **2012**, *5*, 5884. [[CrossRef](#)]
2. Pan, H.; Hu, Y.-S.; Chen, L. Room-temperature stationary sodium-ion batteries for large-scale electric energy storage. *Energy Environ. Sci.* **2013**, *6*, 2338. [[CrossRef](#)]
3. Delmas, C.; Fouassier, C.; Hagenmuller, P. Structural classification and properties of the layered oxides. *Phys. BC* **1980**, *99*, 81–85. [[CrossRef](#)]
4. Yuan, D.; Hu, X.; Qian, J.; Pei, F.; Wu, F.; Mao, R.; Ai, X.; Yang, H.; Cao, Y. P2-type  $\text{Na}_{0.67}\text{Mn}_{0.65}\text{Fe}_{0.2}\text{Ni}_{0.15}\text{O}_2$  cathode material with high-capacity for sodium-ion battery. *Electrochim. Acta* **2014**, *116*, 300–305. [[CrossRef](#)]
5. Kang, W.; Yu, D.Y.W.; Lee, P.-K.; Zhang, Z.; Bian, H.; Li, W.; Ng, T.-W.; Zhang, W.; Lee, C.-S. P2-type  $\text{Na}_x\text{Cu}_{0.15}\text{Ni}_{0.20}\text{Mn}_{0.65}\text{O}_2$  cathodes with high voltage for high-power and long-life sodium-ion batteries. *ACS Appl. Mater. Interfaces* **2016**, *8*, 31661–31668. [[CrossRef](#)]
6. Lee, D.H.; Xu, J.; Meng, Y.S. An advanced cathode for Na-ion batteries with high rate and excellent structural stability. *Phys. Chem. Chem. Phys.* **2013**, *15*, 3304. [[CrossRef](#)]
7. Li, Y.; Yang, Z.; Xu, S.; Mu, L.; Gu, L.; Hu, Y.-S.; Li, H.; Chen, L. Air-stable copper-based P2- $\text{Na}_{7/9}\text{Cu}_{2/9}\text{Fe}_{1/9}\text{Mn}_{2/3}\text{O}_2$  as a new positive electrode material for sodium-ion batteries. *Adv. Sci.* **2015**, *2*, 1500031. [[CrossRef](#)]
8. Yabuuchi, N.; Kajiyama, M.; Iwatate, J.; Nishikawa, H.; Hitomi, S.; Okuyama, R.; Usui, R.; Yamada, Y.; Komaba, S. P2-type  $\text{Na}_x[\text{Fe}_{1/2}\text{Mn}_{1/2}]\text{O}_2$  made from earth-abundant elements for rechargeable Na batteries. *Nat. Mater.* **2012**, *11*, 512–517. [[CrossRef](#)]
9. Sun, X.; Jin, Y.; Zhang, C.-Y.; Wen, J.-W.; Shao, Y.; Zang, Y.; Chen, C.-H.  $\text{Na}[\text{Ni}_{0.4}\text{Fe}_{0.2}\text{Mn}_{0.4-x}\text{Ti}_x]\text{O}_2$ : A cathode of high capacity and superior cyclability for Na-ion batteries. *J. Mater. Chem. A* **2014**, *2*, 17268–17271. [[CrossRef](#)]
10. Vassilaras, P.; Toumar, A.J.; Ceder, G. Electrochemical properties of  $\text{NaNi}_{1/3}\text{Co}_{1/3}\text{Fe}_{1/3}\text{O}_2$  as a cathode material for Na-ion batteries. *Electrochem. Commun.* **2014**, *38*, 79–81. [[CrossRef](#)]
11. Mendiboure, A.; Delmas, C.; Hagenmuller, P. Electrochemical intercalation and deintercalation of  $\text{Na}_x\text{MnO}_2$  bronzes. *J. Solid State Chem.* **1985**, *57*, 323–331. [[CrossRef](#)]
12. Delmas, C.; Braconnier, J.; Fouassier, C.; Hagenmuller, P. Electrochemical intercalation of sodium in  $\text{Na}_x\text{CoO}_2$  bronzes. *Solid State Ion.* **1981**, *3–4*, 165–169. [[CrossRef](#)]
13. Carlier, D.; Cheng, J.H.; Berthelot, R.; Guignard, M.; Yoncheva, M.; Stoyanova, R.; Hwang, B.J.; Delmas, C. The P2- $\text{Na}_{2/3}\text{Co}_{2/3}\text{Mn}_{1/3}\text{O}_2$  phase: Structure, physical properties and electrochemical behavior as positive electrode in sodium battery. *Dalton. Trans.* **2011**, *40*, 9306. [[CrossRef](#)]
14. Manikandan, P.; Heo, S.; Kim, H.W.; Jeong, H.Y.; Lee, E.; Kim, Y. Structural characterization of layered  $\text{Na}_{0.5}\text{Co}_{0.5}\text{Mn}_{0.5}\text{O}_2$  material as a promising cathode for sodium-ion batteries. *J. Power Sources* **2017**, *363*, 442–449. [[CrossRef](#)]
15. Yang, P.; Zhang, C.; Li, M.; Yang, X.; Wang, C.; Bie, X.; Wei, Y.; Chen, G.; Du, F. P2- $\text{NaCo}_{0.5}\text{Mn}_{0.5}\text{O}_2$  as a positive electrode material for sodium-ion batteries. *ChemPhysChem* **2015**, *16*, 3408–3412. [[CrossRef](#)]
16. Bucher, N.; Hartung, S.; Franklin, J.B.; Wise, A.M.; Lim, L.Y.; Chen, H.-Y.; Weker, J.N.; Toney, M.F.; Srinivasan, M. P2- $\text{Na}_x\text{Co}_y\text{Mn}_{1-y}\text{O}_2$  ( $y = 0, 0.1$ ) as cathode materials in sodium-ion batteries-effects of doping and morphology to enhance cycling stability. *Chem. Mater.* **2016**, *28*, 2041–2051. [[CrossRef](#)]
17. Wang, X.; Tamaru, M.; Okubo, M.; Yamada, A. Electrode properties of P2- $\text{Na}_{2/3}\text{Mn}_y\text{Co}_{1-y}\text{O}_2$  as cathode materials for sodium-ion batteries. *J. Phys. Chem. C* **2013**, *117*, 15545–15551. [[CrossRef](#)]
18. Chen, X.; Zhou, X.; Hu, M.; Liang, J.; Wu, D.; Wei, J.; Zhou, Z. Stable layered P3/P2  $\text{Na}_{0.66}\text{Co}_{0.5}\text{Mn}_{0.5}\text{O}_2$  cathode materials for sodium-ion batteries. *J. Mater. Chem. A* **2015**, *3*, 20708–20714. [[CrossRef](#)]
19. Zhu, Y.-E.; Qi, X.; Chen, X.; Zhou, X.; Zhang, X.; Wei, J.; Hu, Y.; Zhou, Z. A P2- $\text{Na}_{0.67}\text{Co}_{0.5}\text{Mn}_{0.5}\text{O}_2$  cathode material with excellent rate capability and cycling stability for sodium ion batteries. *J. Mater. Chem. A* **2016**, *4*, 11103–11109. [[CrossRef](#)]
20. Xu, X.; Ji, S.; Gao, R.; Liu, J. Facile synthesis of P2-type  $\text{Na}_{0.4}\text{Mn}_{0.54}\text{Co}_{0.46}\text{O}_2$  as a high capacity cathode material for sodium-ion batteries. *RSC Adv.* **2015**, *5*, 51454–51460. [[CrossRef](#)]
21. Le Nguyen, M.; Van Nguyen, H.; Ghosh, N.; Garg, A.; Van Tran, M.; Le, P. High-voltage performance of P2- $\text{Na}_x\text{Mn}_{0.5}\text{Co}_{0.5}\text{O}_2$  layered cathode material. *Int. J. Energy Res.* **2021**, *46*, 5119–5133. [[CrossRef](#)]
22. Konarov, A.; Kim, H.J.; Voronina, N.; Bakenov, Z.; Myung, S.-T. P2- $\text{Na}_{2/3}\text{MnO}_2$  by co incorporation: As a cathode material of high capacity and long cycle life for sodium-ion batteries. *ACS Appl. Mater. Interfaces* **2019**, *11*, 28928–28933. [[CrossRef](#)] [[PubMed](#)]
23. Hwang, J.-Y.; Myung, S.-T.; Sun, Y.-K. Sodium-ion batteries: Present and future. *Chem. Soc. Rev.* **2017**, *46*, 3529–3614. [[CrossRef](#)] [[PubMed](#)]
24. Chen, X.; Song, J.; Li, J.; Zhang, H.; Tang, H. A P2/P3 composite-layered cathode material with low-voltage decay for sodium-ion batteries. *J. Appl. Electrochem.* **2021**, *51*, 619–627. [[CrossRef](#)]
25. Shi, Y.; Zhang, Z.; Jiang, P.; Gao, A.; Li, K.; Zhang, Q.; Sun, Y.; Lu, X.; Cao, D.; Lu, X. Unlocking the potential of P3 structure for practical Sodium-ion batteries by fabricating zero strain framework for  $\text{Na}^+$  intercalation. *Energy Storage Mater.* **2021**, *37*, 354–362. [[CrossRef](#)]
26. Zhang, L.; Wang, J.; Li, J.; Schuck, G.; Winter, M.; Schumacher, G.; Li, J. Preferential occupation of Na in P3-type layered cathode material for sodium ion batteries. *Nano Energy* **2020**, *70*, 104535. [[CrossRef](#)]
27. Zhou, Y.-N.; Wang, P.-F.; Zhang, X.-D.; Huang, L.-B.; Wang, W.-P.; Yin, Y.-X.; Xu, S.; Guo, Y.-G. Air-stable and high-voltage layered p3-type cathode for sodium-ion full battery. *ACS Appl. Mater. Interfaces* **2019**, *11*, 24184–24191. [[CrossRef](#)]

28. Lei, Y.; Li, X.; Liu, L.; Ceder, G. Synthesis and stoichiometry of different layered sodium cobalt oxides. *Chem. Mater.* **2014**, *26*, 5288–5296. [[CrossRef](#)]
29. Han, M.H.; Acebedo, B.; Gonzalo, E.; Fontecoba, P.S.; Clarke, S.; Saurel, D.; Rojo, T. Synthesis and electrochemistry study of P2- and O3-phase  $\text{Na}_{2/3}\text{Fe}_{1/2}\text{Mn}_{1/2}\text{O}_2$ . *Electrochim. Acta* **2015**, *182*, 1029–1036. [[CrossRef](#)]
30. Sendova-Vassileva, M.; Stoyanova, R.; Carlier, D.; Yoncheva, M.; Zhecheva, E.; Delmas, C. Raman spectroscopy study on  $\text{Na}_{2/3}\text{Mn}_{1-x}\text{Fe}_x\text{O}_2$  oxides. *Adv. Sci. Technol.* **2010**, *74*, 60–65.
31. Qu, J.F.; Wang, W.; Chen, Y.; Li, G.; Li, X.G. Raman spectra study on nonstoichiometric compound  $\text{Na}_x\text{CoO}_2$ . *Phys. Rev. B* **2006**, *73*, 092518. [[CrossRef](#)]
32. Wang, C.; Yan, J.; Li, T.; Lv, Z.; Hou, X.; Tang, Y.; Zhang, H.; Zheng, Q.; Li, X. A coral-like FeP@NC anode with increasing cycle capacity for sodium-ion and lithium-ion batteries induced by particle refinement. *Angew. Chem. Int. Ed.* **2021**, *60*, 25013–25019. [[CrossRef](#)]
33. Liu, Q.; Hu, Z.; Zou, C.; Jin, H.; Wang, S.; Li, L. Structural engineering of electrode materials to boost high-performance sodium-ion batteries. *Cell Rep. Phys. Sci.* **2021**, *2*, 100551. [[CrossRef](#)]
34. Wang, P.-F.; Yao, H.-R.; Liu, X.-Y.; Zhang, J.-N.; Gu, L.; Yu, X.-Q.; Yin, Y.-X.; Guo, Y.-G. Ti-substituted  $\text{NaNi}_{0.5}\text{Mn}_{0.5-x}\text{Ti}_x\text{O}_2$  cathodes with reversible O3–P3 phase transition for high-performance sodium-ion batteries. *Adv. Mater.* **2017**, *29*, 1700210. [[CrossRef](#)]
35. Yao, H.-R.; Wang, P.-F.; Wang, Y.; Yu, X.; Yin, Y.-X.; Guo, Y.-G. Excellent comprehensive performance of Na-based layered oxide benefiting from the synergetic contributions of multimetal ions. *Adv. Energy Mater.* **2017**, *7*, 1700189. [[CrossRef](#)]
36. Wei, T.-T.; Zhang, N.; Zhao, Y.-S.; Zhu, Y.-R.; Yi, T.-F. Sodium-deficient O3- $\text{Na}_{0.75}\text{Fe}_{0.5-x}\text{Cu}_x\text{Mn}_{0.5}\text{O}_2$  as high-performance cathode materials of sodium-ion batteries. *Compos. Part B Eng.* **2022**, *238*, 109912. [[CrossRef](#)]
37. Wei, T.-T.; Liu, X.; Yang, S.-J.; Wang, P.-F.; Yi, T.-F. Regulating the electrochemical activity of Fe-Mn-Cu-based layer oxides as cathode materials for high-performance Na-ion battery. *J. Energy Chem.* **2023**, *80*, 603–613. [[CrossRef](#)]
38. Bredar, A.R.C.; Chown, A.L.; Burton, A.R.; Farnum, B.H. Electrochemical impedance spectroscopy of metal oxide electrodes for energy applications. *ACS Appl. Energy Mater.* **2020**, *3*, 66–98. [[CrossRef](#)]
39. Costard, J.; Joos, J.; Schmidt, A.; Ivers-Tiffée, E. Charge transfer parameters of  $\text{Ni}_x\text{Mn}_y\text{Co}_{1-x-y}$  cathodes evaluated by a transmission line modeling approach. *Energy Technol.* **2021**, *9*, 2000866. [[CrossRef](#)]
40. Ma, X.; Chen, H.; Ceder, G. Electrochemical properties of monoclinic  $\text{NaMnO}_2$ . *J. Electrochem. Soc.* **2011**, *158*, A1307. [[CrossRef](#)]
41. Zhou, D.; Huang, W.; Lv, X.; Zhao, F. A novel P2/O3 biphasic  $\text{Na}_{0.67}\text{Fe}_{0.425}\text{Mn}_{0.425}\text{Mg}_{0.15}\text{O}_2$  as cathode for high-performance sodium-ion batteries. *J. Power Sources* **2019**, *421*, 147–155. [[CrossRef](#)]
42. Yan, Z.; Tang, L.; Huang, Y.; Hua, W.; Wang, Y.; Liu, R.; Gu, Q.; Indris, S.; Chou, S.-L.; Huang, Y.; et al. A hydrostable cathode material based on the layered P2@P3 composite that shows redox behavior for copper in high-rate and long-cycling sodium-ion batteries. *Angew. Chem.* **2019**, *131*, 1426–1430. [[CrossRef](#)]
43. Liang, X.; Yu, T.-Y.; Ryu, H.-H.; Sun, Y.-K. Hierarchical O3/P2 heterostructured cathode materials for advanced sodium-ion batteries. *Energy Storage Mater.* **2022**, *47*, 515–525. [[CrossRef](#)]
44. Peng, B.; Chen, Y.; Wang, F.; Sun, Z.; Zhao, L.; Zhang, X.; Wang, W.; Zhang, G. Unusual Site-Selective Doping in Layered Cathode Strengthens Electrostatic Cohesion of Alkali-Metal Layer for Practicable Sodium-Ion Full Cell. *Adv. Mater.* **2022**, *34*, 2103210. [[CrossRef](#)] [[PubMed](#)]
45. Wang, H.; Xiao, Y.; Sun, C.; Lai, C.; Ai, X. A type of sodium-ion full-cell with a layered  $\text{NaNi}_{0.5}\text{Ti}_{0.5}\text{O}_2$  cathode and a pre-sodiated hard carbon anode. *RSC Adv.* **2015**, *5*, 106519–106522. [[CrossRef](#)]
46. Jiang, M.; Qian, G.; Liao, X.-Z.; Ren, Z.; Dong, Q.; Meng, D.; Cui, G.; Yuan, S.; Lee, S.-J.; Qin, T.; et al. Revisiting the capacity-fading mechanism of P2-type sodium layered oxide cathode materials during high-voltage cycling. *J. Energy Chem.* **2022**, *69*, 16–25. [[CrossRef](#)]
47. Li, Z.-Y.; Zhang, J.; Gao, R.; Zhang, H.; Hu, Z.; Liu, X. Unveiling the role of Co in improving the high-rate capability and cycling performance of layered  $\text{Na}_{0.7}\text{Mn}_{0.7}\text{Ni}_{0.3-x}\text{Co}_x\text{O}_2$  cathode materials for sodium-ion batteries. *ACS Appl. Mater. Interfaces* **2016**, *8*, 15439–15448. [[CrossRef](#)]
48. Fu, C.C.; Wang, J.; Li, Y.; Liu, G.; Deng, T. Explore the effect of Co doping on P2- $\text{Na}_{0.67}\text{MnO}_2$  prepared by hydrothermal method as cathode materials for sodium ion batteries. *J. Alloys. Compd.* **2022**, *918*, 165569. [[CrossRef](#)]
49. Hou, P.; Li, F.; Wang, Y.; Yin, J.; Xu, X. Mitigating the P2–O2 phase transition of high-voltage P2- $\text{Na}_{2/3}[\text{Ni}_{1/3}\text{Mn}_{2/3}]\text{O}_2$  cathodes by cobalt gradient substitution for high-rate sodium-ion batteries. *J. Mater. Chem. A* **2019**, *7*, 4705–4713. [[CrossRef](#)]
50. Rahman, M.M.; Mao, J.; Kan, W.H.; Sun, C.-J.; Li, L.; Zhang, Y.; Avdeev, M.; Du, X.-W.; Lin, F. An ordered P2/P3 composite layered oxide cathode with long cycle life in sodium-ion batteries. *ACS Mater. Lett.* **2019**, *1*, 573–581. [[CrossRef](#)]
51. Zhou, Y.-N.; Wang, P.-F.; Niu, Y.-B.; Li, Q.; Yu, X.; Yin, Y.-X.; Xu, S.; Guo, Y.-G. A P2/P3 composite layered cathode for high-performance Na-ion full batteries. *Nano Energy* **2019**, *55*, 143–150. [[CrossRef](#)]
52. Zhang, Y.; Kim, S.; Feng, G.; Wang, Y.; Liu, L.; Ceder, G.; Li, X. The interaction between Cu and Fe in P2-type  $\text{Na}_x\text{TMO}_2$  cathodes for advanced battery performance. *J. Electrochem. Soc.* **2018**, *165*, A1184–A1192. [[CrossRef](#)]
53. Mortemard de Boisse, B.; Carlier, D.; Guignard, M.; Bourgeois, L.; Delmas, C. P2- $\text{Na}_x\text{Mn}_{1/2}\text{Fe}_{1/2}\text{O}_2$  phase used as positive electrode in Na batteries: Structural changes induced by the electrochemical (de)intercalation process. *Inorg. Chem.* **2014**, *53*, 11197–11205. [[CrossRef](#)]

54. Singh, G.; Tapia-Ruiz, N.; Lopez del Amo, J.M.; Maitra, U.; Somerville, J.W.; Armstrong, A.R.; Martinez de Ilarduya, J.; Rojo, T.; Bruce, P.G. High voltage Mg-doped  $\text{Na}_{0.67}\text{Ni}_{0.3-x}\text{Mg}_x\text{Mn}_{0.7}\text{O}_2$  ( $x = 0.05, 0.1$ ) Na-ion cathodes with enhanced stability and rate capability. *Chem. Mater.* **2016**, *28*, 5087–5094. [[CrossRef](#)]
55. Or, T.; Kaliyappan, K.; Bai, Z.; Chen, Z. High voltage stability and characterization of P2- $\text{Na}_{0.66}\text{Mn}_{1-y}\text{Mg}_y\text{O}_2$  cathode for sodium-ion batteries. *ChemElectroChem* **2020**, *7*, 3284–3290. [[CrossRef](#)]
56. Risthaus, T.; Chen, L.; Wang, J.; Li, J.; Zhou, D.; Zhang, L.; Ning, D.; Cao, X.; Zhang, X.; Schumacher, G.; et al. P3  $\text{Na}_{0.9}\text{Ni}_{0.5}\text{Mn}_{0.5}\text{O}_2$  cathode material for sodium ion batteries. *Chem. Mater.* **2019**, *31*, 5376–5383. [[CrossRef](#)]

**Disclaimer/Publisher's Note:** The statements, opinions and data contained in all publications are solely those of the individual author(s) and contributor(s) and not of MDPI and/or the editor(s). MDPI and/or the editor(s) disclaim responsibility for any injury to people or property resulting from any ideas, methods, instructions or products referred to in the content.